Applied Catalysis B: Environmental 243 (2019) 502–512

Contents lists available at ScienceDirect

Applied Catalysis B: Environmental

journal homepage: www.elsevier.com/locate/apcatb

# Experimental and DFT insights of the Zn-doping effects on the visible-light photocatalytic water splitting and dye decomposition over Zn-doped BiOBr photocatalysts

Junqiu Guo[a], Xin Liao[a], Ming-Hsien Lee[b], Geoff Hyett[c], Chung-Che Huang[d], Daniel W. Hewak[d], Sakellaris Mailis[d], Wei Zhou[a,e], Zheng Jiang[a,*]

[a] School of Engineering, Faculty of Engineering and Physical Sciences, University of Southampton, Southampton SO17 1BJ, UK
[b] Department of Physics, Tamkang University, Taipei 25137, Taiwan, ROC
[c] School of Chemistry, Faculty of Engineering and Physical Sciences, University of Southampton, Southampton SO17 1BJ, UK
[d] Optoelectronics Research Centre, Faculty of Engineering and Physical Sciences, University of Southampton, Southampton SO17 1BJ, UK
[e] Key Laboratory of Functional Inorganic Material Chemistry, Ministry of Education of PR China, Heilongjiang University, Harbin 150080, PR China

ARTICLE INFO

*Keywords:*
Photocatalysis
Zn-doped BiOBr
Photoelectrochemistry
Band structure
DFT

ABSTRACT

Synergetic experimental and DFT insights of energy band structures and photogenerated rate-limiting reactive species are indispensable to design impurity-doped photocatalysts for photocatalytic environment remediation and solar fuels. Herein, despite the larger bandgap (Eg) of the Zn-doped BiOBr samples, they exhibited superior activity to BiOBr in the photocatalytic water splitting but impaired the photodegradation of Rhodamine B under visible-light illumination. Based on the spectral and electrochemical impedance characterisations and DFT simulations, the wider bandgaps of Zn-doped BiOBr samples were explicitly assigned to the more positive valence band maxima (VBM) and more negative conduction band minima (CBM). The enhanced photocatalytic water splitting on the Zn-doped BiOBr was arisen from the higher redox chemical potentials of charge carriers on respective CBM and VBM, suppressed back reactions and depressed recombination of photogenerated charge carriers. However, the reduced $e^-$-$h^+$ recombination on the Zn-doped BiOBr cannot cancel the detrimental influences from the weaker light absorption and dye-sensitisation effects, leading to slower RhB photodegradation.

## 1. Introduction

The ever-increasing concerns of energy and environment sustainability have recently motivated great enthusiasm in the photocatalytic environment remediation and artificial photosynthesis that require the rational design of effective visible-light photocatalysts and the understanding of their working mechanism. The bismuth oxybromide (BiOBr) compound semiconductor has emerged recently as a stable and active visible-light photocatalyst with an indirect bandgap of 2.6–2.9 eV [1–3]. The BiOBr is of a tetragonal crystal structure, constructed by alternative stacks of $[Bi_2O_2]^{2+}$ slabs and double $Br^-$ slabs through Van de Waals interaction. Between the constituent $[Bi_2O_2]^{2+}$ and $2[Br^-]$ slabs, there exist intrinsic built-in static electric fields. Such built-in electric fields were thought able to promote separation of photogenerated electrons ($e^{-1}$) and holes ($h^+$) across CBM and VBM [4–6] and to benefit their transportation to catalyst surface for participating redox reactions or to depress recombination otherwise [7–9]. In order to further modulate the bandstructure and promote surface photocatalysis of BiOBr, heteroatom doping [1,10–17] or surface hybridisation with small-bandgap semiconductors or metal nanoparticles [18–21] were attempted successfully. Moreover, the heterogeneous photocatalysis usually involves multiple active species, including photogenerated charge carriers ($e^{-1}$ and $h^+$) and derived reactive species, though their respective roles in the photocatalysis are under debating [10,22]. For instance of photocatalytic dye degradation, the photoexcited dye can transfer $e^{-1}$ or $h^+$ to CBM or VBM of the semiconductor photocatalysts, though the dye-sensitisation effects were not paid enough attention when assessing the performance of photocatalysts [8,23]. Therefore, it is pivotal to unravel the relevance of photocatalysis with bandstructure and photogenerated reactive species for proposing a reasonable photocatalysis mechanism [24,25].

Compared to the surface metallisation and hybridisation, doping

* Corresponding author.
*E-mail address:* z.jiang@soton.ac.uk (Z. Jiang).

https://doi.org/10.1016/j.apcatb.2018.09.089
Received 24 May 2018; Received in revised form 21 September 2018; Accepted 28 September 2018
Available online 01 October 2018
0926-3373/ © 2018 Published by Elsevier B.V.

BiOBr with heteroatom is very convenient for practical applications [10,19,26,27] because doping to BiOBr can occur even at ambient conditions. In comparison to partial substitution of Br or O via mono- or co-doping of Cl, I, N or S [10,14], the substitutions of Bi by metal are redeemed more flexible to tune the optoelectrical and catalytic properties of Bi-based oxyhalides (BiOX) [4,10,12,13,15,28]. As for the roles of metal dopants, previous DFT simulations suggested transition metal or rare earth dopants (eg, Ti, Fe, Mn, Eu, etc) with unclosed *d* and *f* valance electrons can introduce midgap energy levels in the bandstructure of pristine bismuth oxyhalides (BiOX, X = Cl, Br, I) [5,6,29,30]. However, Zn possesses closed $3d^{10}$ and $4s^2$ electronic states that are supposed to alter the bandstructure of BiOBr distinctive from other metallic dopants as mentioned above, so that particular attention was paid to Zn-doped BiOBr in this work.

Although enhanced visible-light photodegradation of RhB was observed on the flower-like Zn-doped BiOBr, which was attributed to their large surface areas and enhanced $e^-$-$h^+$ separation [16], the results need further interpretation in terms of the charge carriers or active species. Controversially, Zn-doped BiOBr (Zn-BiOBr) displayed lower activity in photodegradation of RhB and 2-chlorophenol than BiOBr, which was attributed to the dopant cations capture of photoelectrons based reactive hydroxyl radical ($^{\cdot}OH^-$) [31]. Using the widely adopted semi-empirical electronegativity methods [3,10,27,32,33], the latter research also illustrated the bandstructure of BiOBr and Zn-BiOBr with suitable CBMs and VBMs that enable dye decomposition and water splitting. These controversial results further motivated us to examine Zn-doping effects on the RhB photodegradation and water splitting.

Because the CBM and VBM are pivotal for interpreting photocatalytic dye degradation and solar fuels [34], it is necessary to gain in-depth insights of the Zn-doping effects on the bandstructures of BiOBr and Zn-doped BiOBr. The insights can be achieved by comparing the experimental bandstructures (from spectral and photoelectromistry characterisations) and those simulated using the state-of-the-art DFT code based on first principle theory [4–6,28,30]. Combined UV–vis spectral techniques, both the X-ray photoelectronic spectrum (XPS) and photoelectrochemical characterisations have been evidenced effective and reliable to analyse energy band positions (Mott-Schottky Impedance Spectra) and $e^-$-$h^+$ separation efficiency (chronoamperometry) [8,35]. Moreover, photocatalytic experiments using suitable radical scavengers allow to identify the rate-limit reactive species in photocatalysis [36].

In this work, Zn-doped BiOBr samples were prepared and applied in photodegradation of RhB and water splitting. The pristine BiOBr and Zn-doped BiOBr with 1/8 and 1/16 fractions of Bi atoms substituted by Zn were comparatively characterised and simulated by DFT to gain explicit insights into Zn-doping effects. Using radical scavengers, the research also distinguished the effects of bandgap, reactive radicals and dye sensitisation on photocatalytic RhB degradation and water splitting.

## 2. Computational and experimental

### 2.1. Computational details

The electronic structures of typical BiOBr and xZn-BiOBr samples were simulated using DFT method implementing CASTEP 16.1 code [37]. The supercells of the primitive BiOBr cell were applied to build the Zn-doped BiOBr crystal models, where one Zn atom substitution of one Bi atom in the (2 × 2 × 1) and (2 × 2 × 2) supercells will create the respective original models of 1/8Zn-BiOBr (illustrated in Fig. 1 as an example) and 1/16Zn-BiOBr, corresponding to 1.04 and 2.08 atm% doping levels.

In the simulation, GGA-PBE exchange-correlation functional and norm-conserving pseudopotentials were used for geometry optimisation and electronic structure calculations, with considerations of the electron spin polarization. For the geometry optimisation using BFGS method, the energy cut-off for the plane wave expansion was set to be 750 eV, resulting in a convergence of total energy and residual force tolerance to be within 0.1 eV/atom and $2.0 \times 10^{-6}$ eV/angstrom, respectively. The *k*-point Monkhorst-Pack (MP) spacing of 0.125/Å was adopted when sampling in the first Brillouin zones for geometry optimisation of the primitive BiOBr and the Zn-doped BiOBr supercells, while the *k*-point MP spacing of 0.0125/Å was adopted for band structure and density of states (DOS) calculations. The band structures were calculated along the Monkhorst-Pack (MP) grid connecting the high-symmetry k-points of Z (0,0,0.5), A (0.5,0.5,0.5), M (0.5,0.5,0), Γ (0,0,0), Z (0,0,0.5), R (0,0.5,0.5), X (0,0.5,0) and Γ (0,0,0) in the *k*-space of the first Brillouin zone, where the two Γ points were applied because the MP grid should be closed.

### 2.2. Preparation of the Zn-doped BiOBr photocatalysts and photoelectrodes

The Zn-doped BiOBr photocatalysts with varying Zn-doping levels ($Zn_xBi_{(1-x)}OBr$, hereafter denoted as xZn-BiOBr, where x is the Zn-doping level) were prepared via a simple co-precipitation method. Typically, under rigorous stirring, 20 mL KBr (0.2 M)/NaOH (0.2 M) mixed solution was poured into 20 mL 20% acetic acid aqueous solution containing calculated amount of $Bi(NO_3)_3$ and $Zn(NO_3)_2$, where the Zn/Bi/Br molar ratios of x:(1-x):1 were maintained for obtaining xZn-BiOBr samples. Upon mixing the above solutions, pale yellowish precipitates were observed immediately, and the systems' final pH was adjusted to 12.0 using 0.3 M NaOH solution. The resulting mixtures were stirring for 6 h and ageing overnight before filtration and washing thoroughly by deionised water (DI). The received wet gels were dried in oven under 60 °C for 24 h to obtain the xZn-BiOBr photocatalysts.

The photoelectrodes of xZn-BiOBr photocatalysts were fabricated by doctor-blade coating of the photocatalyst pastes onto clean ITO/glass slices (1.5 cm × 1.5 cm, resistance of 15Ω/sq) which were pre-washed alternatively by absolute ethanol and DI water under ultrasonication (40 kHz, 5 min each). The pastes of the photocatalysts were prepared by mixing 0.1 g photocatalysts with 100 μL ethanol/water (3:1) solution. 10 μL of photocatalyst paste was dropped on the dry clean ITO/glass fixed on flat bench using scotch tape to expose $1 \times 1.5\ cm^2$ area, and then slowly rolled a clean glass rod to cast the film. The casted films were then dried at 60 ℃ for 24 h before photoelectrochemistry tests.

### 2.3. Characterisations

All the X-ray diffraction data were collected from the Rigaku SmartLab X-ray diffractometer, using Cu-Kα1 radiation (λ = 0.154056 nm) and a scan rate of 0.05° 2θ/s, to determine the crystal phases of the samples. The UV–vis diffuse reflectance spectra were obtained on Perkin Elmer Lambda 950 UV/Vis/NIR spectrophotometer equipped with a 150 mm snap-in integrating sphere for capturing diffuse and specular reflectance, where $BaSO_4$ was used as standard reflectance. The acquired lattice parameters and bandgap energies were listed in Table 1.

X-ray photoelectron spectroscopy (XPS) was performed on a Thermo Scientific Escaplab 250 K-alpha photoelectron spectrometer using monochromatic Al-Kα radiation. Survey and Valence band spectra were collected in the range 0–1100 eV (binding energy) at pass energy of 160 eV. Peak positions were calibrated to carbon and fitted using CasaXPS software. The morphologies of the samples were measured on JSM59 SEM manufactured by JEOL on which Energy Dispersive X-Ray (EDX) analyser was installed to analyse the composition of specimens in question.

### 2.4. Photocatalytic degradation of RhB and water splitting

The photodegradation of Rhodamine B (RhB) on the as-prepared samples was performed at ambient temperature under visible-light irradiation. A 300 W Xe lamp equipped with a 400 nm cut-off filter to

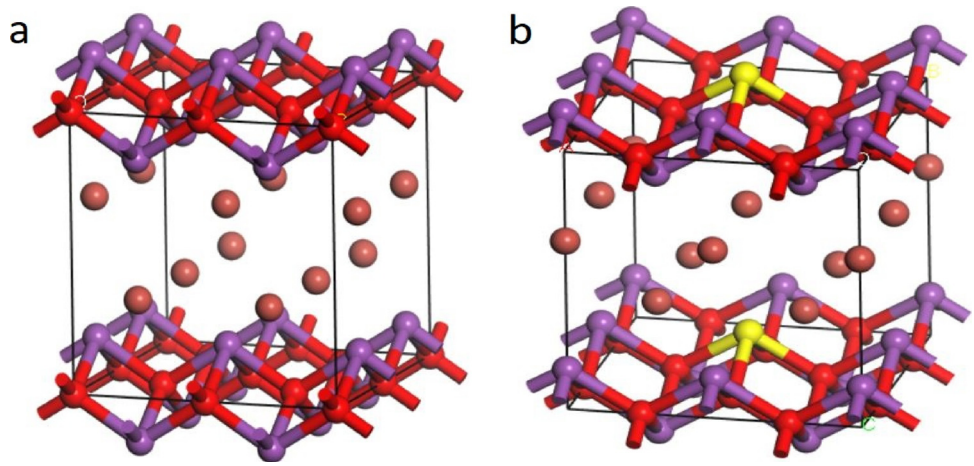


**Fig. 1.** The ball-stick crystal models of BiOBr (2 × 2 × 1) supercell (a) and the derived 1/8Zn-doped BiOBr (b), where the purple, red, brown and yellow balls refer to Bi, O, Br and Zn atoms. (For interpretation of the references to colour in this figure legend, the reader is referred to the web version of this article).

**Table 1**
Experimental and computed lattice parameters and bandgap of pure and Zn-doped BiOBr.

| | a = b/Å | c/Å | c/a | V/Å$^3$ | $E_g$/eV |
|---|---|---|---|---|---|
| BiOBr_Exp | 3.7573 | 9.7672 | 2.5995 | 137.6224 | 2.42 |
| | 3.8377 | 9.4045 | 2.4506 | 138.5089 | 2.60 |
| 1/16 Zn-BiOBr | 3.7421 | 9.2882 | 2.4821 | 130.0656 | 2.76 |
| | 3.8133 | 9.3998 | 2.4650 | 136.6849 | 2.67 |
| 1/8 Zn-BiOBr | 3.7273 | 9.3503 | 2.5086 | 129.9015 | 2.87 |
| | 3.7945 | 9.3595 | 2.4666 | 134.7602 | 2.88 |

*Note*: the DFT simulated lattice parameters, cell volume and bandgap (Eg) were listed in the lower rows of individual samples, while the experimental results were derived from XRD characterisations and UV–vis spectra, respectively.

remove UV light was used as light source, irradiating atop with light intensity of 30 mW/cm$^2$ and 15 cm distance away from the beaker containing photocatalyst and RhB aqueous solution. In a typical photocatalysis experiment, 0.1 g of the photocatalyst powder was dispersed into 100 mL 20 ppm RhB aqueous solution. Before light irradiation, the mixed system was remained in dark for one hour to establish RhB adsorption-desorption equilibrium on catalyst surface. The initial concentration ($C_0$) was defined as the concentration of RhB upon adsorption-desorption equilibrium rather than the original concentration of RhB solution because the photocatalysis occurs on catalyst surface. In order to determine the temporal RhB concentration ($C_t$) at certain photo-reaction time (t) during photocatalysis, 4 mL liquid suspension was taken out every 3 min. and centrifuged under 6000 rmp to obtain supernatant solution for sampling by a UV–vis spectrophotometer (PerkinElmer Lampda 750 s). Since photodegradation of dilute RhB in the aqueous solution is a pseudo-first-order reaction, the apparent kinetic coefficient ($k$) can be calculated form using the equation below:

$$-\ln\left(\frac{C_t}{C_0}\right) = kt \tag{1}$$

Radical scavenging experiments were conducted to identify the rate-limiting reactive species. Because ethylenediaminetetraacetic acid (EDTA), isopropanol (IPA) and p-benzoquinone (p-BQ) are effective scavengers with respective to $h^+$ at VBM, hydroxyl radical ($^{\cdot}OH$) and superoxygen radical due to $e^-$ at CBM, they were mixed into RhB solution respectively to acquire corresponding photodegradation activities for comparing and assessing the contributions of photogenerated $e^-$ [38] and $h^+$ [39] at band edges into photodegradation.

The experiments of photocatalytic hydrogen from water splitting were carried out in the similar procedure presented in the previous report [35]. Briefly, 100 mg of as-prepared photocatalysts was taken into a homemade reactor containing 80 mL deionized water and 20 mL methanol, to which $H_2PtCl_6{\cdot}6H_2O$ (0.5 wt% to photocatalysts) was added as a co-catalyst. Before photocatalytic testing, the reactor and the entire gas circulating system were de-aerated using a vacuum pump for 30 min. All photocatalytic $H_2$ generation tests were under continuous illumination using an Autolight CEL-HXF300 xenon lamp (300 W, 100 mW/cm$^2$) equipped with optical cut-off filters to realize visible light irradiation. The photocatalytic $H_2$ production was determined using Agilent gas chromatography (GC, 7900) at the sampling interval of 60 min per test.

### 2.5. Photoelectrochemistry tests

Photoelectrochemistry measurements of the as-prepared BiOBr and Zn-doped BiOBr photoelectrodes were carried out at room temperature in a standard three-electrode cell using the AUTOLAB PGSTAT 302N equipped with FRA spectroscopy. The as-prepared film electrodes, a platinum disk and a saturated calomel electrode (SCE) were used as working electrodes, counter electrode and reference electrode, respectively. The electrolyte supporting solution was 100 mL 0.5 M $Na_2SO_4$ solution with constant pH of 6.5. The Mott-Schottky (M–S) data were acquired at the optimised frequency of 3000 Hz in dark, with 10 mV/s scan rate and 10 mV AC amplitude. The acquired potentials were transformed to reversible hydrogen electrode scale (RHE) to pH of 0.

The quantitative analysis of M-S data to acquire flat band potential ($V_{fb}$) is based on the Mott-Schottky law from the plots of $C_{sc}^{-2}$ versus the applied potential bias ($V_{app}$):

$$\frac{1}{C_{sc}^2} = \frac{2}{A^2\varepsilon_0\varepsilon_r e N_d}\left(V_{app} - V_{fb} - \frac{k_B T}{e}\right) \tag{2}$$

where $C_{sc}$, A, $N_d$, $\varepsilon_r$ and $\varepsilon_0$ are respective to the space capacitance, electrode area (1.0 cm$^2$ in this work), donor density, relative dielectric of semiconductor and vacuum dielectric, while the $k_B$, T and $e$ stand for the Boltzmann constant ($1.38 \times 10^{-23}$ J/K), system absolute temperature (293 K here) and charge of electron ($1.602 \times 10^{-19}$ C), respectively. Extrapolation linear M-S plot to potential bias axis leads to an interception potential ($V_{extro}$, the corresponding charge energy of $E_{extro} = e{\cdot}V_{extro}$), while the slope of the M–S straight plot ($k_{M\text{-}S}$) is proportional inversely to the density of majority carriers ($N_d$, e- and $h^+$ for n-type and p-type semiconductor, respectively) [40]. The acquired $E_{extro}$ can be manipulated by the following equations (the inferences were detailed in the ESI) to gain band edges in the RHE scale.

$$E_{fb\sim SCE} = E_{extro} - k_B T/e \tag{3}$$

**Table 2**
Photodegradation rate constants and energy band edges (eV) of pure and Zn-doped BiOBr samples.

| Photocatalysts | Rate constants ($min^{-1}$) | $E_{extro\sim SCE}$ | $E_{fb\sim RHE}$ | $E_{CBM\sim RHE}$ | $E_{VBM\sim RHE}$ | M-S Slope ($k_{M\text{-}S}$) |
|---|---|---|---|---|---|---|
| BiOBr | 0.1528 | −0.45V | 0.15 | −0.05V | 2.37 (2.35) | $0.9570 \times 10^9$ |
| 1/16Zn-BiOBr | 0.1357 | −0.56V | 0.04 | −0.16V | 2.60 (2.55) | $3.7783 \times 10^9$ |
| 1/8Zn-BiOBr | 0.1028 | −0.62V | −0.02 | −0.22V | 2.65 (2.61) | $3.2109 \times 10^9$ |

*Note*: The bracketed numbers in $E_{VBM\sim RHE}$ column were retrieved from VBM XPS spectra.

$$E_{fb\sim RHE} = E_{fb\sim SCE} + E^0_{SCE\sim RHE} + \frac{RT}{nF}pH \quad (4)$$

$$E_{CBM} = E_{fb\sim RHE} - 0.2eV \quad (5)$$

$$E_{VBM} = E_{CBM} + Eg \quad (6)$$

The Eqs. (3)–(4) were applied to calibrate the potential contributions from temperature T (by $\frac{k_B T}{e}$ in Eq. (3)) and pH (by $\frac{RT}{nF}pH$ in Eq. (4)), where R, n and F represent the universal gas constant, the number of electrons involved in the electrode reaction and the Faraday constant, respectively. In the Eq. (5), 0.2 eV was applied because the CBM potential is typical 0.2 V more negative than flat-band for most n-type semiconductors [40,41]. The Eg, $E_{CBM}$ and $E_{VBM}$ are bandgap, energy positions of CBM and VBM, respectively. The retrieved data of BiOBr and the Zn-doped BiOBr were listed in Table 2.

The chronoamperometry tests (I-t plots) were recorded at light on-off cycle operation (on-off time interval of 20 s) at open circuit potentials ($V_{OC}$). The photocurrents acquired from $Na_2SO_4$ electrolyte solution containing RhB were applied to assess the dye-sensitisation effects. The corresponding chronoamperometrical results were summarised in Table 3.

## 3. Result and discussion

### 3.1. Crystal structure and surface composition

Fig. 2 presents the XRD data of the BiOBr and Zn-doped BiOBr samples, where all the characteristic diffraction peaks of the samples can be indexed to the tetragonal phase BiOBr (JCPDS 73-2061), without ZnO diffraction observed [11]. The gradual shifts of characteristic diffraction peaks suggest that Zn was incorporated into the BiOBr matrix and caused distortion of BiOBr lattice [11], which agrees with the smaller inter-plane spacing distance as shown in the HRTEM image of 1/16Zn-BiOBr (Fig. S1). The lattice parameters of BiOBr and Zn-doped BiOBr samples derived from XRD data are summarised in Table 1, further revealing that the Zn-doping induces shrinking of lattice parameters and distorts crystal structure. The unit cell shrinkages of the Zn-doped BiOBr samples can be assigned to the substitutions of larger $Bi^{3+}$

**Table 3**
Temporal photocurrents on the pristine and Zn-doped BiOBr photoelectrodes.

| Photocatalysts | Photocurrent density (J, μA/cm$^2$)[a] | | | |
|---|---|---|---|---|
| | $J_{PC}$ | $J_{RhB/PC}$ | $\Delta J$[b] | $\Delta J/J_{PC}$ (%)[c] |
| BiOBr | 0.32 | 0.51 | 0.19 | +59.4% |
| 1/16Zn-BiOBr | 0.19 | 0.30 | 0.11 | +57.9% |
| 1/8Zn-BiOBr | 0.13 | 0.21 | 0.08 | +61.5% |

*Note*:
[a] The photocurrent density (J) data were collected at $V_{OC}$ of corresponding photoelectrode, where $J_{PC}$ and $J_{RhB/PC}$ represent J values acquired in 0.5 M $Na_2SO_4$ without and with 20 ppm RhB solution, respectively.
[b] The absolute photocurrent density enhancement due to dye-sensitisation, $\Delta J = J_{RhB/PC} - J_{PC}$.
[c] The relative enhancement in percentage due to dye-sensitisation, calculated by $\Delta J/J_{PC}$ *100%.

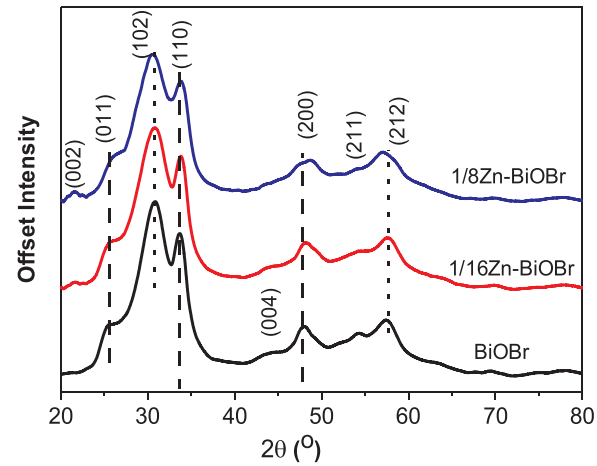


**Fig. 2.** The XRD patterns of BiOBr and Zn-doped BiOBr samples.

(1.03 Å) by smaller $Zn^{2+}$ cation (radius of 0.74 Å) [42], which is in good agreement with DFT optimised geometric data and those of previous report [16].

X-ray photoemission spectroscopy (XPS) was applied to analyse the surface elementary composition, the chemistry environment and the electronic interaction of BiOBr and Zn-doped BiOBr samples. The XPS survey spectra and core level XPS (Figs. S2 and S3) indicate that the samples with designed chemical composition were successfully prepared, in good agreement with the composition data acquired by EDS spectra (Fig. S4). Fig. 3(a–d) shows the fitted core level XPS spectra corresponding to the Bi 4f, O 1s, Br 3d and Zn 2p core electron binding energies, which evidences cationic Zn was incorporated into BiOBr and systematically altered elemental binding energies (B.E.). The attributions of the core level XPS were presented in the electronic supporting information (ESI, S3). More importantly, the significant and systematic red shifts of Bi, O, Br binding energies (Fig. 3a–c) are observed from the core-level XPS spectra of Zn-doped BiOBr, which are owing to the fact that Zn-dopant donated electrons to adjacent more electronegative Bi, O, Br atoms and thus enhanced their core electron densities. The red-shifts of Br 3d binding energy may be partly arisen from the weakened Van de Walls forces between the $[Zn_{2x}Bi_{2\text{-}2x}O_2]^{(2-x)+}$ and $Br^-$ slabs as $Zn^{2+}$ substituting $Bi^{3+}$. The blue shifts of Zn 2p XPS (Fig. 3d), as increasing Zn-doping levels, support the electron donation effects of Zn-dopant.

### 3.2. Optoelectronic properties

The UV–vis diffuse reflection absorbance spectra (UV–vis-DRS) and corresponding Tauc plots of the photocatalysts were presented in Fig. 4 to compare their light absorption properties and gain bandgap energies. In a broad wavelength region up to 600 nm, BiOBr exhibits stronger light absorption than Zn-doped BiOBr samples (Fig. 4a), suggesting that the increase of Zn-doping level caused gradual blue-shifts of the absorbance edges. However, the significant drifts in the absorbance spectra in high wavelength, which are due to the hue and specular reflection of the samples, hindered deriving accurate bandgap energies. To overcome such spectral problem, the UV–vis-DRS spectra were

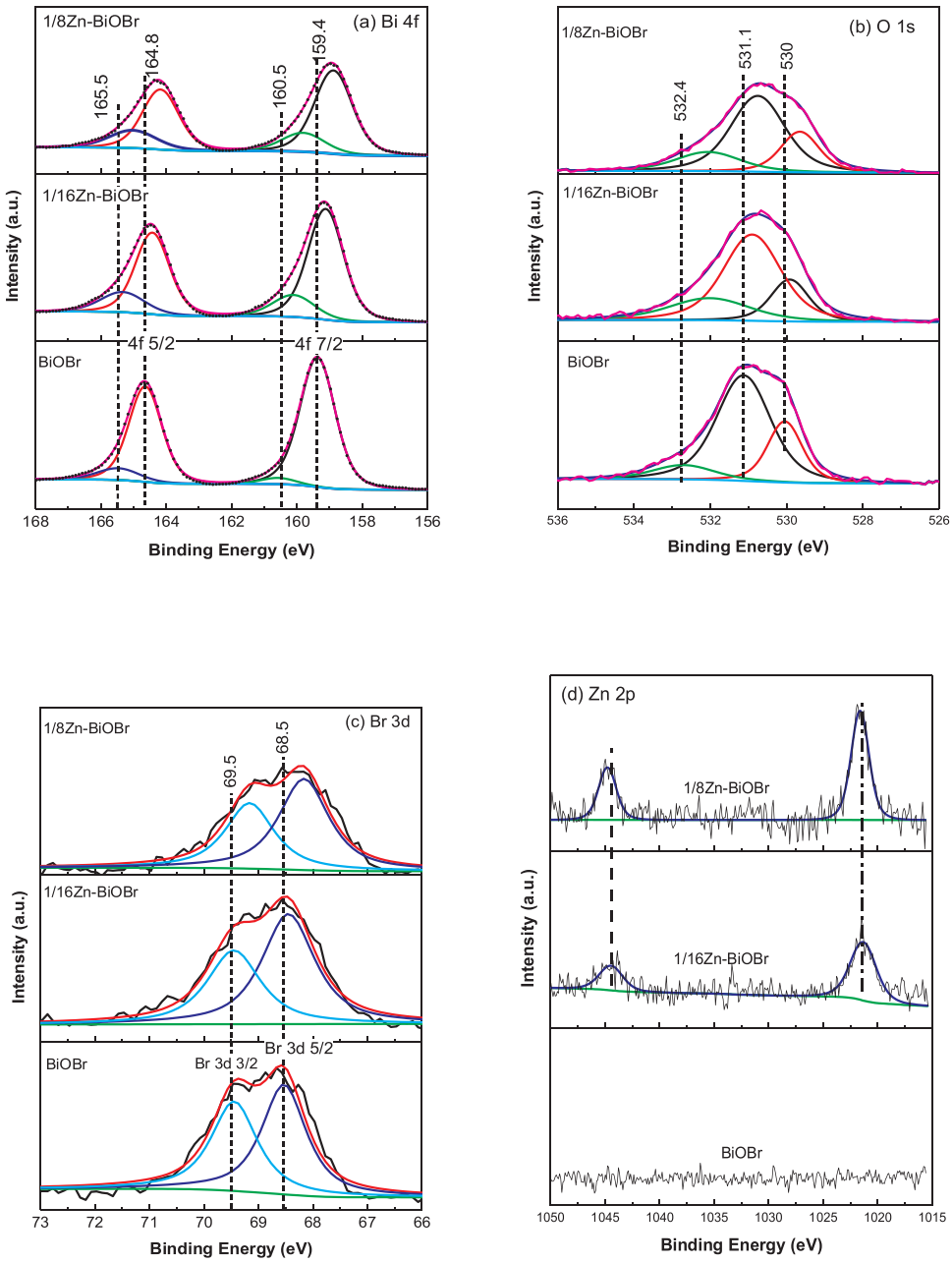


**Fig. 3.** Core level XPS of Bi 4f (a), O1s (b), Br 3d(c), Zn 2p (d) of BiOBr and Zn-doped BiOBr samples.

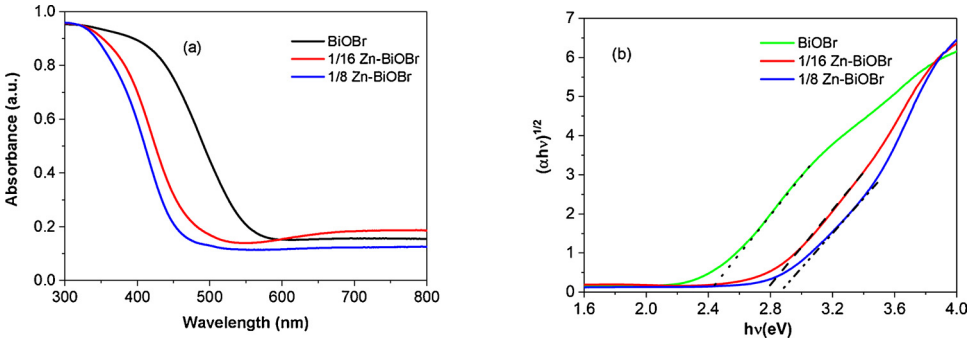


**Fig. 4.** The UV–vis absorbance (a) and tauc plots (b) of BiOBr and Zn-doped BiOBr samples.

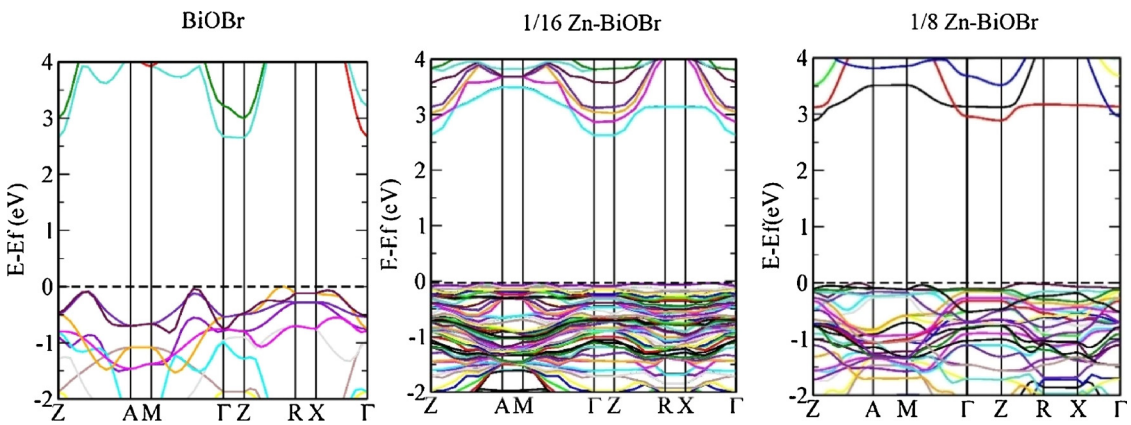


**Fig. 5.** The DFT-simulated bandstructure of the BiOBr, 1/16Zn-BiOBr and 1/8Zn-BiOBr.

transformed into Tauc plots (Fig. 4b) implementing Kubelka-Munk equation. It was found Zn-doping did not change the indirect transition characteristic of BiOBr, as accordance with DFT calculations (see Fig. 5). The derived optical bandgap (Eg) of BiOBr is 2.42 eV, smaller than those of the 1/16Zn-BiOBr (2.74 eV) and 1/8Zn-BiOBr (2.87 eV). The results suggest that Zn-doping broadens the bandgap of BiOBr. Although the Eg of our BiOBr is consistent with that of BiOBr samples prepared using CTAB-directed synthesis [31], the influences of Zn-doping on bandgaps of the samples in our work are different from those of the Zn-doped BiOBr nano-flowers synthesised by solvothermal method [16]. Their smaller bandgaps of Zn-BiOBr nanoflowers are presumably due to their hierarchical structure and their structural defects because reductive organic solvent was involved in that work [16].

The electronic structures of the materials were simulated implementing GGA-PBE exchange-correlation functional embedded in the CASTEP16.1 DFT code. As shown in Fig. 5, the computed electronic band-structures of BiOBr and Zn-doped BiOBr samples are projected in the first Brillion zone. It should be noted the Fermi energy levels in Fig. 5 were set at the top of VBM for convenience. One can see that the electronic states at VBM and CBM of the Zn-doped BiOBr samples are less dispersive (smaller curvature) than those of BiOBr, suggesting their corresponding VBM $h^+$ and CBM $e^-$ are heavier and less active because the charge effective and mobility are directly proportional to the band wave curvature. In addition, the computed Eg values of the Zn-doped BiOBr samples are larger than that of BiOBr, in good consistence with experimental data (Table 1) [5,6], which concretely support the experimental findings that Zn-doping broadens bandgaps.

In contrast, previous DFT research revealed that the metal-dopants with partially occupied *d* or *f* shells can narrow the bandgap of BiOBr due to the impurity-induced mid-gaps [4,28]. No impurity mid-gaps are observed in the band gap regions of our Zn-BiOBr materials, because the electrons on closed *3d* orbitals of Zn are not interactive enough to bring electronic states to bandgaps. Zn $3d^{10}$ electrons are found mainly contributing to deeper bands, localising at ~7 eV more positive (deeper) than VBM (Fig. S5). The total electron density of states (DOS) and Zn partial DOS (PDOS), as shown in Fig. S6, further confirming the negligible contributions of Zn 3*d* orbitals to bandgaps.

Furthermore, the simulated CB and VB band edges suggest that the Zn-doping can alter the bandgap transition path of BiOBr (Fig. 5). Within the first Brillion zone, the conduction band minima (CBMs) of the BiOBr and Zn-doped BiOBr samples all locate at Z points, whereas Zn-doping leads to valance band maxima (VBMs) gradually shift from R towards Z point that shortens the indirect transition path. The calculated optical transitions well match the transition features shown in the UV–vis spectra (Fig. 4b): increasing Zn-doping levels decreases tangents (slopes) of the Tauc plots in bandgap zones.

The total DOS and PDOS of pristine and Zn-doped BiOBr materials (Fig. 6) further reveal the effects of Zn-doping on the band structure. As shown in Fig. 6a, the CB and CBM of BiOBr are predominated by Bi 6*p* state, while the VB and VBM are mainly occupied by Br 4*p* state with significant hybridisation with O 2*p* and Bi 6*s* electron states [5,6]. In contrast, for the Zn-doped BiOBr (Figs. 6b and S5–6), the CBM of Zn-doped BiOBr is dominated by Zn 4*s* electron states which are of stronger density and hybridise with the low-density Bi 6*p* state slightly above CBM. In addition, the Zn-doping changes the electronic density and components of the VB and VBM, exhibiting slightly lower density of Br 4p, O 2p and Bi 6s states than those of BiOBr.

The Zn-dopant also broadens VB width, which was evidenced experimentally by the broader VB XPS of Zn-doped BiOBr (Fig. 6d). Comparing the XPS near to VBMs of the samples (Fig. 6d), one can conclude that Zn-doping pushes the VBM to deeper energy level (more positive), namely higher oxidation potential of VB holes. By extrapolating the valence band edge of the VBM XPS, the VBM potentials are determined to be 2.05 eV, 2.25 eV and 2.31 eV for BiOBr, 1/16Zn-BiOBr and 1/8Zn-BiOBr, respectively. Since the XPS spectra were calibrated by C 1s XPS ($E_f$ of C is ~0.3 eV vs RHE), VBM potentials can then be transferred to 2.35, 2.55 and 2.61 eV in RHE scale, agreeing with those from Mott-Schottky EIS measurements (Fig. 7). In addition, compared to BiOBr, Zn-doped BiOBr samples show lower XPS intensity of their VBM edges, which is due to the Zn-dopant reducing electronic density of Br 3*d*, O 2*p* and Bi 6*s* states, as suggested by DOS results (Fig. 6a–c).

Fig. 7a shows the Mott-Schottky (M-S) plots of the BiOBr and Zn-doped BiOBr photoanodes, where the positive slopes of the linear regions reveal they are n-type semiconductors [43]. The tangent gradients ($k_{M\text{-}S}$) of the M-S linear plots of the samples become greater as increasing Zn-doping levels (Table 2), suggesting their VB electron donor density ($N_d$) drops because $k_{M\text{-}S}$ is inversely proportional to majority density (electron for n-type semiconductors) [44]. The results well agree with the computed bandstructures and DOS of the Zn-doped BiOBr samples, in which the flatter band edges suggest less dispersion of electrons ($e^-$) or heavier $h^+$ occupy the VBMs [6].

The $E_{fb\sim RHE}$, $E_{CBM}$ and $E_{VBM}$ of the samples, extracted from the M-S plots and referred to RHE scale, are listed in Table 2. Accordingly, the energetic band diagrams of BiOBr and Zn-doped BiOBr samples can be drawn, as illustrated in Fig. 7b. One can see that increasing the Zn-doping level of Zn-BiOBr samples raise their CBMs to higher levels (more negative) but push VBMs downwards (more positive), so as to broaden the bandgap (Eg). The acquired VBM potentials from M-S plots are consistent with those from VBM XPS, validating the M-S characterisation is an effective and reliable method to define the chemical potentials of VBM.

### 3.3. Photocatalytic water splitting and RhB decomposition

The band diagrams presented in Fig. 7b suggest the BiOBr and Zn-doped BiOBr can photocatalyticalyse water splitting [45].

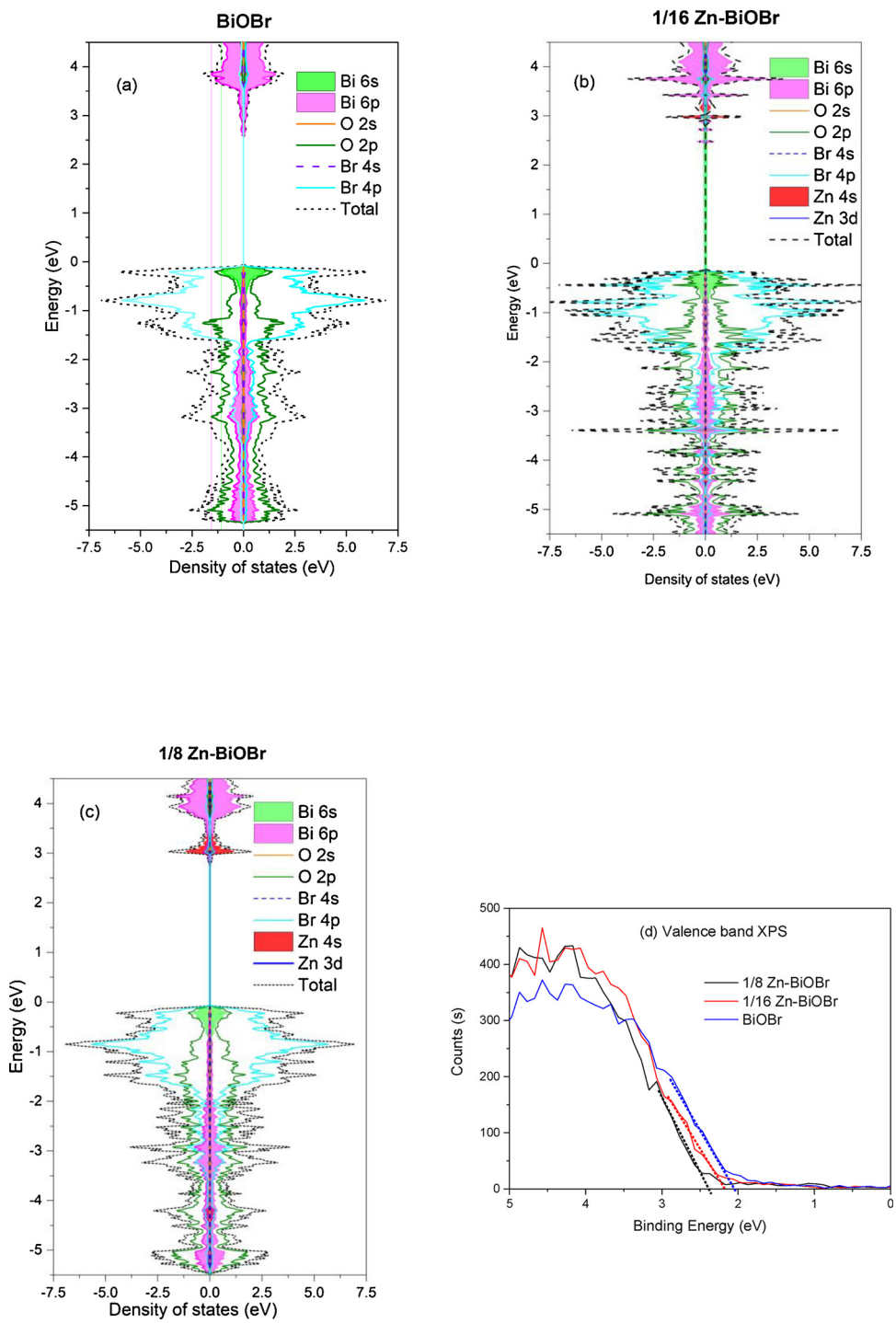


**Fig. 6.** DOS and PDOS of BiOBr (a), 1/16Zn-BiOBr (b) and 1/8Zn-BiOBr (c), where DOS of Bi and Zn are shadowed, and the VBM XPS of pristine and Zn-doped BiOBr samples (d) 1/8Zn-BiOBr and 1/16Zn-BiOBr.

Experimentally, higher photocatalytic hydrogen evolution rate was acquired (Fig. 8a) on the 1/16Zn-BiOBr (~29 μmol/g/h) with respect to BiOBr (~13 μmol/g/h). Considering the weaker PL intensity of 1/16Zn-BiOBr (Fig. S7) than that of BiOBr, the enhanced water splitting on 1/16Zn-BiOBr can be assigned to the stronger redox ability (Fig. 7b) and the suppressed recombination of the photogenerated charge carriers. The hydrogen evolution results also suggest that the promoted photogenerated charge carriers cancelled the influences from weaker light adsorptions of Zn-BiOBr samples than BiOBr.

Fig. 8b comparatively shows the apparent photocatalysis kinetics of visible-light-driven photodegradation of RhB on BiOBr and the Zn-doped BiOBr samples. Since the samples displayed similar adsorption-desorption equilibrium (Fig. S8) and thus almost identical specific surface areas (SSA), their apparent kinetic coefficients can be used to compare their microscopic kinetic behaviour. The derived apparent kinetic coefficients ($k$, Table 2) suggest the RhB photodegradation rate is dragged as Zn-doping levels increasing, which agrees with their apparent activity of RhB photodegradation (black lines in Fig. 8c and Fig. S9). Therefore, the stronger light adsorption of BiOBr seems responsible for its higher photocatalytic activity than that of the Zn-doped samples, though such interpretation cannot clarify the mechanistic responsibility of the dye-sensitisation and photoexcitons for the redox half reactions.

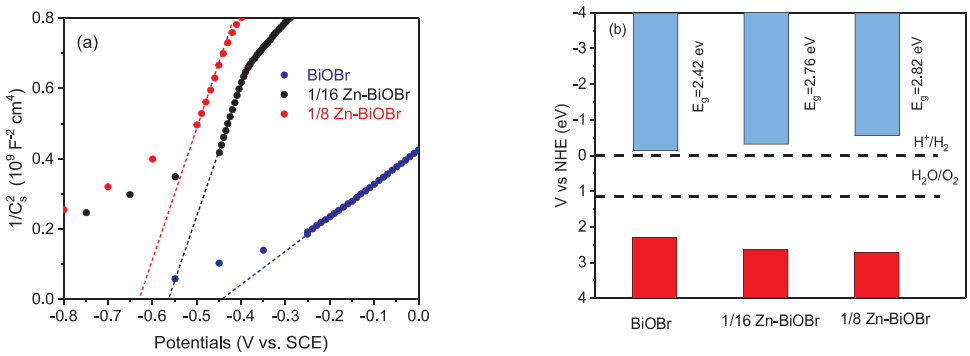


**Fig. 7.** The photoanode Mott-Schottky plots (a) and the derived energy band diagrams vs RHE at pH = 0 (b) of the BiOBr and Zn-doped BiOBr samples.

## 4. Mechanism perspectives of photocatalysis in RhB photodegradation and $H_2$ evolution

It is a great challenge to unravel the photocatalytic mechanism in the aqueous photocatalytic system, because it contains multiple aqueous radical active species, in particular the hydroxyl radical ($HO^{\cdot}$, 1.99 eV vs RHE), $H_2O_2$ (1.77 eV vs RHE) and superoxygen radicals ($^{\cdot}O_2^{-}$, −0.046 eV vs RHE) [3]. The radicals possess strong redox power and can compete with $e^-$ and $h^+$ from excited photocatalysts or dye. Comparing the redox potentials of the aqueous radicals with band edges of the photocatalysts (Fig. 7 b and Table 2), redox potentials of LUMO and HOMO of the excited RhB and $H^+$, the major elementary reactions involved in the photocatalytic reactions are proposed, as illustrated in Fig. 9.

### 4.1. Mechanism interpretation of H2 evolution

From the chemical potential point of view, the bandstructure of BiOBr and Zn-BiOBr photocatalysts (Fig.7 and Fig. 9a) imply they can enable $H_2$ evolution from the methanol-sacrificial water splitting systems. On one hand, chemical potentials of photogenerated $e^-$ from CBs of BiOBr and Zn-BiOBr photocatalysts are more negative than the $H^+$ reduction potential ($E_{H^+/H2}$ = 0 eV *vs* RHE) (Fig. 9a), so $H_2$ is able to release in the absence of other $e^-$ scavengers (i.e. dissolved $O_2$) apart from $H^+$. On the other hand, methanol can largely scavenge $h^+$ accumulated on the surface of the BiOBr-based photocatalysts, which facilitates $e^-$ transferring to catalyst surface for $H^+$ reduction. It is noteworthy that the I-t plot (Fig. 10a) is not effective to interpret water splitting because methanol wasn't used in the chronoamperometry tests.

The enhanced photocatalytic $H_2$ evolution due to Zn-doping can be

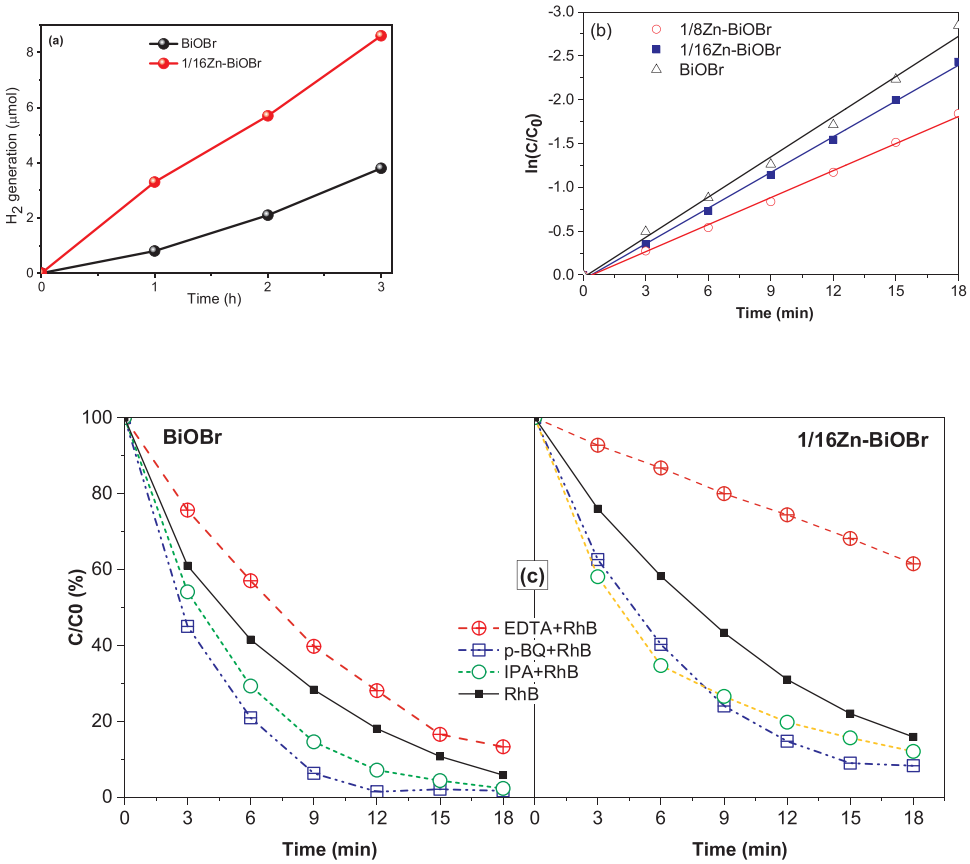


**Fig. 8.** Visible-light photocatalytic water splitting (a) and RhB photodegradation on BiOBr and Zn-BiOBr samples: (b) apparent kinetic curves and (c) effects of adding radical scaverngers.

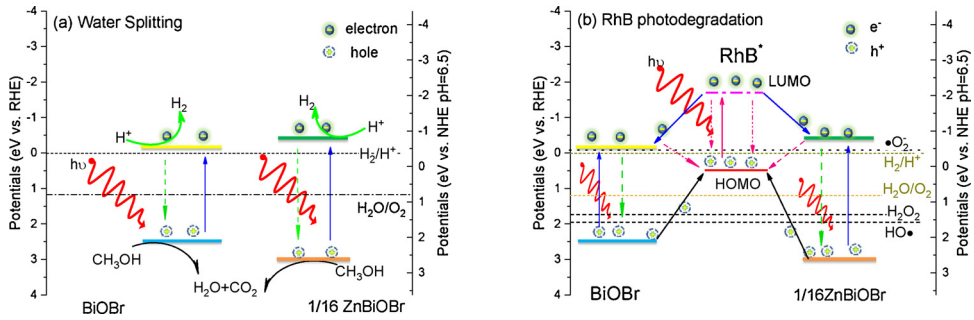


**Fig. 9.** The schematic mechanisms of photocatalytic water splitting (a) and RhB degradation (b) on the prestine and Zn-doped BiOBr samples.

interpreted from bandstructure and $e^-$-$h^+$ recombination aspects. From the thermodynamic point of view, the $H_2$ evolution on Zn-BiOBr is more favourable, because the potential energy difference ($\Delta E_{CBM\sim H^+/H2} = E_{CBM} - E_{H^+/H2}$) between $E_{CBM}$ and $E_{H^+/H2}$ on Zn-BiOBr is more negative than $\Delta E_{CBM\sim H^+/H2}$ on the BiOBr. The potential energy difference is the driving force to promote electron transfer and the photogeneration of $H_2$: first, the photogenerated $e^-$ at CBM of 1/16Zn-BiOBr is more reductive ($E_{CBM}$ more negative, Fig. 9a) than that of BiOBr. The more negative $\Delta E_{CBM\sim H^+/H2}$ of the 1/16Zn-BiOBr is helpful to limit the back reaction of $H^+$ reduction. Second and more importantly, the $e^-$-$h^+$ recombination of BiOBr is nearly four-fold that of 1/16Zn-BiOBr as reflected by their PL spectra (Fig. S7). Such strong recombination on BiOBr would mitigate its advantageous light absorption. Therefore, the higher reductive of CBM $e^-$, limited back reaction and the greater amount of reactive $e^-$ are responsible for the superior $H_2$ evolution on 1/16Zn-BiOBr to pristine BiOBr.

### 4.2. Mechanism interpretation of RhB photodegradation

For the energy downhill photodegradation of RhB, the competition of photoexcitons ($e^-$-$h^+$) at band edges of photocatalysts with the relevant radical derivatives as well as the roles of dye photosensitisation can be defined from the critical analyses of the radical scavenger and chronoamperometry experiments.

#### 4.2.1. Rate-limiting species in RhB photodegradation

As comparatively shown in the Fig. 8c, photocatalytic activities on the pristine and Zn-doped BiOBr samples are found being enhanced significantly as adding either $^{\cdot}O_2^-$ scavenger (p-BQ) or $HO^{\cdot}$ (isopropanol, IPA) into respective RhB photodegradation systems [46]. These results roughly rule out that $^{\cdot}O_2^-$ and $HO^{\cdot}$ radicals limit the RhB photodegradation rate, because these radicals were consumed rapidly by scavengers so that led to enhanced availability of photogenerated $h^+$. The p-BQ and IPA quenching experiments also reflect that the photogenerated holes are probably the rate-limiting species. Indeed, the vital rate-determining roles of $h^+$ were evidenced by the dramatically declined RhB degradation activity when adding EDTA-Na ($h^+$ scavenger) [16].

In the photocatalytic system, $^{\cdot}O_2^-$ should be related to the photogenerated electrons at the CBMs of BiOBr and Zn-BiOBr samples because their CBMs are more negative than $^{\cdot}O_2^-$ formation energy (Fig. 9b). Taking account of the more negative LUMO of RhB (−1.77 eV vs RHE) than their CBMs [47], the photogenerated electrons at CBMs can be injected from both excited RhB (photosensitisation effects) and excited photocatalysts. Since the the HOMO of RhB* (~0.47 eV vs RHE) is more positive than $^{\cdot}O_2^-$ formation energy (−0.05 eV), the recombination between the $h^+$ at HOMO of RhB* and $^{\cdot}O_2^-$ can be occurred. However, the p-BQ can quench $^{\cdot}O_2^-$ in the RhB photodegradation system, which restrains the recombination and promotes the VBM $h^+$, hence, one can observe the p-BQ enhanced the RhB photodegradation.

The IPA enhanced RhB photodegradation likely follows the same mechanism if the photogenerated $HO^{\cdot}$ radicals are induced by $e^-$ from CBMs of the photocatalysts (Fig. 9b). Because the $HO^{\cdot}$ radical is more energetically positive than HOMO of RhB* but more negative than holes at photocatalysts VBMs, the $HO^{\cdot}$ radicals can accept $h^+$ from VBMs rather than from the HOMO of RhB*. However, IPA quenched the $HO^{\cdot}$ radicals, which consumes more electrons and reduces their recombination with $h^+$ at VBMs, so that the IPA-enhanced RhB photodegradation was observed on all the BiOBr-based samples (Fig. 8c).

The addition of EDTA caused more significant decline of the RhB photodegradation rate on the 1/16Zn-BiOBr sample than the pristine BiOBr, indicating their VBM holes are rate-limiting species and play more important roles in the RhB photodegradation on Zn-BiOBr than BiOBr. This is reasonable because the VBMs of Zn-BiOBr are more positive, namely holes more oxidative, than those of BiOBr and RhB HOMO (Fig. 9b). However, the light absorption on 1/16Zn-BiOBr is weaker than BiOBr and its total effective photogenerated holes exclusive recombined are still in larger quantity than that of BiOBr (Fig.9a), so that its apparent RhB photogeneration activity is lower than that of BiOBr. Although the above apparent photocatalysis and scavenger experiments can roughly define the roles of reactive species, the

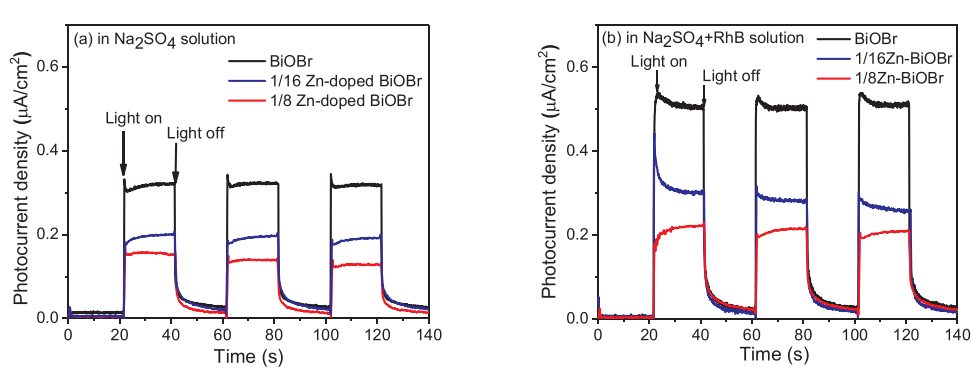


**Fig. 10.** Temporary photocurrent density acquired on the BiOBr and Zn-doped BiOBr photoelectrodes in $Na_2SO_4$ electrolyte solutions without (a) and with 20 ppm RhB (b).

RhB photosensitisation effects remains insufficiently quantified.

#### 4.2.2. RhB dye photosensitisation effects

The dye photosensitisation effects on the RhB photocatalytic degradation over the BiOBr-based photocatalysts were evaluated by chronoamperometrical experiments at open circuit potentials ($V_{OC}$). Fig. 10 shows the acquired temporary photocurrent density against light on-off time (J-t plots) of the BiOBr-based photoelectrodes in 0.5 M $Na_2SO_4$ electrolyte solutions without (Fig. 10a) and with (Fig. 10b) 20 ppm RhB (denoted as $J_{PC}$ and $J_{RhB/PC}$, respectively). The photocurrent density can reflect the charges effectively separated and transferred at the photocatalysts surfaces. Apparently, the RhB photosensitisations dramatically promote the photocurrent density on all the BiOBr and Zn-doped BiOBr samples, with 57%–62% enhancements ($\Delta J/J_{PC}$ x100%). As listed in Table 3, although the relative enhancement ratios are comparable as increasing Zn-doping levels, their quantified absolute photocurrent density enhancements ($\Delta J$) due to dye photosensitisation declines. The smaller enhancement of absolute photocurrent density on the Zn-BiOBr suggests Zn-doping weakens RhB photosensitisation effects, which is another crucial factor results in their lower photodegradation.

## 5. Conclusion

The Zn-doping effects on RhB photodegradation over Zn-doped BiOBr, synthesised via a simple alkaline co-precipitation method, were convincingly defined from the perspectives of potential energy and the reactive radical species through the comprehensive spectral, DFT and photoelectrochemical investigations on the crystal structure, optoelectronic properties and photoelectrocatalysis of pristine and Zn-doped BiOBr. Under visible-light illumination, the Zn-doping led to superior $H_2$ evolution activity of Zn-BiOBr to BiOBr but detrimental RhB photodegradation.

The experimental and DFT characterisations of BiOBr and Zn-doped BiOBr samples revealed that Zn-doping shrinks the lattice of BiOBr though Zn-doped BiOBr samples remain indirect optical transitions in their bandgap regions. Distinct from the doping effects of other metals of unclosed *d* or *f* outermost electron states, the Zn-doping in BiOBr broadens the bandgap by enhancing CBM and deepening VBM of BiOBr: The CBMs of Zn-doped BiOBr mainly compose of Zn 4*s* electron state with slight hybridisation with more negative Bi 6*p* state (which predominates the CBM of BiOBr), while the VBMs of Zn-doped BiOBr, composed of Br 3d, O 2p and Bi 6s states, are very similar to that of BiOBr except for the reduced density due to Zn-doping. Because the closed Zn $3d^{10}$ electrons locate in deeper band, they exert negligible influences on the VBM of Zn-BiOBr smaples but the Zn-dopant donates electrons to the surrounding atoms as reflected by core level XPS characterisations.

In the methanol-sacrificial photocatalytic systems, the enhanced water splitting on Zn-BiOBr is here attributed to the more reactive charge carriers at band edges, the reduced back reaction of proton photo-reduction and the recombination of charge carriers on the 1/16Zn-doped BiOBr, which altogether contribute more than light absorption for $H_2$ evolution. In contrast, the rate-limiting reactive species are photogenerated holes on the BiOBr-based materials in spite of multiple reactive radicals involving in the complex dye photodegradation system. The detrimental RhB photodegradation activities on Zn-doped BiOBr samples are convincingly attributed to Zn-doping that weakens light absorption, reduces dye-sensitisation effects and the density of surface photogenerated charge carriers.

## Acknowledgements

This work was partially supported by the Zipler Institute seed grant at University of Southampton, the UK Newton Fund International Collaboration (NRCP1415/261) and the UK Royal Society International collaboration awards (IECNSFC170670 and IE160277). JG and XL appreciate the Eustice studentship from the University of Southampton. For DFT simulation, the authors acknowledge the use of the IRIDIS High Performance Computing Facility and associated support services at the University of Southampton, in the completion of this work.

## Appendix A. Supplementary data

Supplementary material related to this article can be found, in the online version, at doi:https://doi.org/10.1016/j.apcatb.2018.09.089.

## References

[1] D.S. Bhachu, S.J.A. Moniz, S. Sathasivam, D.O. Scanlon, A. Walsh, S.M. Bawaked, M. Mokhtar, A.Y. Obaid, I.P. Parkin, J. Tang, C.J. Carmalt, Bismuth oxyhalides: synthesis, structure and photoelectrochemical activity, Chem. Sci. 7 (2016) 4832–4841.
[2] J. Shang, W. Hao, X. Lv, T. Wang, X. Wang, Y. Du, S. Dou, T. Xie, D. Wang, J. Wang, Bismuth oxybromide with reasonable photocatalytic reduction activity under visible light, ACS Catal. 4 (2014) 954–961.
[3] Z. Jiang, F. Yang, G. Yang, L. Kong, M.O. Jones, T. Xiao, P.P. Edwards, The hydrothermal synthesis of BiOBr flakes for visible-light-responsive photocatalytic degradation of methyl orange, J. Photochem. Photobiol. A 212 (2010) 8–13.
[4] Z.Y. Zhao, W.W. Dai, Structural, electronic, and optical properties of Eu-doped BiOX (X = F, Cl, Br, I): a DFT + U study, Inorg. Chem. 53 (2014) 13001–13011.
[5] W.L. Huang, Electronic structures and optical properties of BiOX (X = F, Cl, Br, I) via DFT calculations, J. Comput. Chem. 30 (2009) 1882–1891.
[6] W.L. Huang, Q. Zhu, DFT calculations on the electronic structures of BiOX (X = F, Cl, Br, I) photocatalysts with and without semicore Bi 5d states, J. Comput. Chem. 30 (2009) 183–190.
[7] J. Wang, N. Tafen de, J.P. Lewis, Z. Hong, A. Manivannan, M. Zhi, M. Li, N. Wu, Origin of photocatalytic activity of nitrogen-doped TiO2 nanobelts, J. Am. Chem. Soc. 131 (2009) 12290–12297.
[8] A.S. Alshammari, L. Chi, X. Chen, A. Bagabas, D. Kramer, A. Alromaeh, Z. Jiang, Visible-light photocatalysis on C-doped ZnO derived from polymer-assisted pyrolysis, RSC Adv. 5 (2015) 27690–27698.
[9] A. Dash, S. Sarkar, V.N. Adusumalli, V. Mahalingam, Microwave synthesis, photoluminescence, and photocatalytic activity of PVA-functionalized Eu3 + -doped BiOX (X = Cl, Br, I) nanoflakes, Langmuir: ACS J. Surf. Colloids 30 (2014) 1401–1409.
[10] C. Bi, J. Cao, H. Lin, Y. Wang, S. Chen, Tunable photocatalytic and photoelectric properties of I − -doped BiOBr photocatalyst: dramatic pH effect, RSC Adv. 6 (2016) 15525–15534.
[11] Z. Liu, B. Wu, Y. Zhao, J. Niu, Y. Zhu, Solvothermal synthesis and photocatalytic activity of Al-doped BiOBr microspheres, Ceram. Int. 40 (2014) 5597–5603.
[12] M.Q. He, W.B. Li, J.X. Xia, L. Xu, J. Di, H. Xu, S. Yin, H.M. Li, M.N. Li, The enhanced visible light photocatalytic activity of yttrium-doped BiOBr synthesized via a reactable ionic liquid, Appl. Surf. Sci. 331 (2015) 170–178.
[13] R.J. Wang, G.H. Jiang, X.H. Wang, R.B. Hu, X.G. Xi, S.Y. Bao, Y. Zhou, T. Tong, S. Wang, T. Wang, W.X. Chen, Efficient visible-light-induced photocatalytic activity over the novel Ti-doped BiOBr microspheres, Powder Technol. 228 (2012) 258–263.
[14] G.H. Jiang, X. Li, Z. Wei, X.H. Wang, T.T. Jiang, X.X. Du, W.X. Chen, Immobilization of N, S-codoped BiOBr on glass fibers for photocatalytic degradation of rhodamine B, Powder Technol. 261 (2014) 170–175.
[15] Z. Wei, G.H. Jiang, L. Shen, X. Li, X.H. Wang, W.X. Chen, Preparation of Mn-doped BiOBr microspheres for efficient visible-light-induced photocatalysis, MRS Commun. 3 (2013) 145–149.
[16] X.C. Song, Y.F. Zheng, H.Y. Yin, J.N. Liu, X.D. Ruan, The solvothermal synthesis and enhanced photocatalytic activity of Zn2 + doped BiOBr hierarchical nanostructures, New J. Chem. 40 (2016) 130–135.
[17] G.H. Jiang, X.H. Wang, Z. Wei, X. Li, X.G. Xi, R.B. Hu, B.L. Tang, R.J. Wang, S. Wang, T. Wang, W.X. Chen, Photocatalytic properties of hierarchical structures based on Fe-doped BiOBr hollow microspheres, J. Mater. Chem. A 1 (2013) 2406–2410.
[18] L. Ye, J. Liu, C. Gong, L. Tian, T. Peng, L. Zan, Two different roles of metallic Ag on Ag/AgX/BiOX (X = Cl, Br) visible light photocatalysts: surface plasmon resonance and Z-Scheme bridge, ACS Catal. 2 (2012) 1677–1683.
[19] C. Yu, C. Fan, X. Meng, K. Yang, F. Cao, X. Li, A novel Ag/BiOBr nanoplate catalyst with high photocatalytic activity in the decomposition of dyes, React. Kinet. Mech. Catal. 103 (2011) 141–151.
[20] L. Lu, L. Kong, Z. Jiang, H.H.C. Lai, T. Xiao, P.P. Edwards, Visible-light-driven photodegradation of rhodamine B on Ag-modified BiOBr, Catal. Lett. 142 (2012) 771–778.
[21] L. Kong, Z. Jiang, H.H.C. Lai, T. Xiao, P.P. Edwards, Does noble metal modification improve the photocatalytic activity of BiOCl? Prog. Nat. Sci.: Mater. Int. 23 (2013) 286–293.
[22] D. Jiang, L. Chen, J. Zhu, M. Chen, W. Shi, J. Xie, Novel p-n heterojunction photocatalyst constructed by porous graphite-like C3N4 and nanostructured BiOI: facile synthesis and enhanced photocatalytic activity, Dalton Trans. 42 (2013) 15726–15734.
[23] S.K. Poznyak, A.I. Kulak, Photoelectrochemical properties of bismuth oxyhalide films, Electrochim. Acta 35 (1990) 1941–1947.

[24] F.E. Osterloh, Photocatalysis versus photosynthesis: a sensitivity analysis of devices for solar energy conversion and chemical transformations, ACS Energy Lett. 2 (2017) 445–453.
[25] K. Takanabe, Photocatalytic water splitting: quantitative approaches toward photocatalyst by design, ACS Catal. 7 (2017) 8006–8022.
[26] H. Cheng, B. Huang, Y. Dai, Engineering BiOX (X = Cl, Br, I) nanostructures for highly efficient photocatalytic applications, Nanoscale 6 (2014) 2009–2026.
[27] L. Kong, Z. Jiang, H.H. Lai, R.J. Nicholls, T. Xiao, M.O. Jones, P.P. Edwards, Unusual reactivity of visible-light-responsive AgBr–BiOBr heterojunction photocatalysts, J. Catal. 293 (2012) 116–125.
[28] X.C. Zhang, C.M. Fan, Y.W. Wang, Y.F. Wang, Z.H. Liang, P.D. Han, DFT + U predictions: the effect of oxygen vacancy on the structural, electronic and photocatalytic properties of Mn-doped BiOCl, Comput. Mater. Sci. 71 (2013) 135–145.
[29] D.M. Jang, I.H. Kwak, E.L. Kwon, C.S. Jung, H.S. Im, K. Park, J. Park, Transition-metal doping of oxide nanocrystals for enhanced catalytic oxygen evolution, J. Phys. Chem. C 119 (2015) 1921–1927.
[30] Z.Y. Zhao, Q.L. Liu, W.W. Dai, Structural, electronic, and optical properties of BiOX1-xYx (X, Y = F, Cl, Br, and I) solid solutions from DFT calculations, Sci. Rep. 6 (2016) 31449.
[31] W. Li, Y. Zou, X. Geng, F. Xiao, G. An, D. Wang, Constructing highly catalytic oxidation over BiOBr-based hierarchical microspheres: Importance of redox potential of doped cations, Mol. Catal. 438 (2017) 19–29.
[32] L. Kong, Z. Jiang, T. Xiao, L. Lu, M.O. Jones, P.P. Edwards, Exceptional visible-light-driven photocatalytic activity over BiOBr-ZnFe2O4 heterojunctions, Chem. Commun. (Camb.) 47 (2011) 5512–5514.
[33] G. Jiang, R. Wang, X. Wang, X. Xi, R. Hu, Y. Zhou, S. Wang, T. Wang, W. Chen, Novel highly active visible-light-induced photocatalysts based on BiOBr with Ti doping and Ag decorating, ACS Appl. Mater. Interfaces 4 (2012) 4440–4444.
[34] C. Piliego, M. Manca, R. Kroon, M. Yarema, K. Szendrei, M.R. Andersson, W. Heiss, M.A. Loi, Charge separation dynamics in a narrow band gap polymer-PbS nanocrystal blend for efficient hybrid solar cells, J. Mater. Chem. 22 (2012) 24411–24416.
[35] K. Zhang, W. Zhou, L. Chi, X. Zhang, W. Hu, B. Jiang, K. Pan, G. Tian, Z. Jiang, Black N/H-TiO2 nanoplates with a flower-like hierarchical architecture for photocatalytic hydrogen evolution, ChemSusChem 9 (2016) 2841–2848.
[36] T. Tan, D. Beydoun, R. Amal, Effects of organic hole scavengers on the photocatalytic reduction of selenium anions, J. Photochem. Photobiol. A 159 (2003) 273–280.
[37] S.J. Clark, M.D. Segall, C.J. Pickard, P.J. Hasnip, M.I.J. Probert, K. Refson, M.C. Payne, First principles methods using CASTEP, Zeitschrift fur Kristallographie 220 (2005) 567–570.
[38] Y. Kato, R. Nagao, T. Noguchi, Redox potential of the terminal quinone electron acceptor QB in photosystem II reveals the mechanism of electron transfer regulation, Proc. Natl. Acad. Sci. U. S. A. 113 (2016) 620–625.
[39] H.T. Hsu, S.S. Chen, Y.F. Tang, H.C. Hsi, Enhanced photocatalytic activity of chromium(VI) reduction and EDTA oxidization by photoelectrocatalysis combining cationic exchange membrane processes, J. Hazard. Mater. 248–249 (2013) 97–106.
[40] J.H. Kennedy, Flatband potentials and donor densities of polycrystalline α-Fe[sub 2]O[sub 3] determined from Mott-Schottky plots, J. Electrochem. Soc. 125 (1978) 723.
[41] S.R. Morrison, Electrochemistry at Semiconductor and Oxidized Metal Electrodes, Plenum Press, 1980.
[42] R.D. Shannon, Revised effective ionic-radii and systematic studies of interatomic distances in halides and chalcogenides, Acta Crystallogr. A 32 (1976) 751–767.
[43] P. Kwolek, K. Szacilowski, Photoelectrochemistry of n-type bismuth oxyiodide, Electrochim. Acta 104 (2013) 448–453.
[44] K. Gelderman, L. Lee, S.W. Donne, Flat-band potential of a semiconductor: using the Mott–Schottky equation, J. Chem. Educ. 84 (2007) 685.
[45] X.Y. Kong, W.P.C. Lee, W.-J. Ong, S.-P. Chai, A.R. Mohamed, Oxygen-deficient biobr as a highly stable photocatalyst for efficient CO2 reduction into renewable carbon-neutral fuels, ChemCatChem 8 (2016) 3074–3081.
[46] Q. Liu, Y.R. Guo, Z.H. Chen, Z.G. Zhang, X.M. Fang, Constructing a novel ternary Fe (III)/graphene/g-C3N4 composite photocatalyst with enhanced visible-light driven photocatalytic activity via interfacial charge transfer effect, Appl. Catal. B-Environ. 183 (2016) 231–241.
[47] H. Zhao, Y. Zhang, G. Li, F. Tian, H. Tang, R. Chen, Rhodamine B-sensitized BiOCl hierarchical nanostructure for methyl orange photodegradation, RSC Adv. 6 (2016) 7772–7779.